

Accepted Manuscript

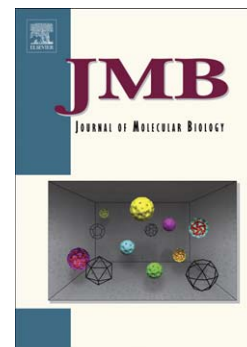
Monitoring ligand-induced protein ordering in drug discovery

Christy R. Grace, David Ban, Jaeki Min, Anand Mayasundari, Lie Min, Kristin E. Finch, Lyra Griffiths, Nagakumar Bharatham, Donald Bashford, R. Kiplin Guy, Michael A. Dyer, Richard W. Kriwacki

PII: S0022-2836(16)00035-8
DOI: doi: [10.1016/j.jmb.2016.01.016](https://doi.org/10.1016/j.jmb.2016.01.016)
Reference: YJMBI 64970

To appear in: *Journal of Molecular Biology*

Received date: 17 November 2015
Revised date: 15 January 2016
Accepted date: 18 January 2016



Please cite this article as: Grace, C.R., Ban, D., Min, J., Mayasundari, A., Min, L., Finch, K.E., Griffiths, L., Bharatham, N., Bashford, D., Kiplin Guy, R., Dyer, M.A. & Kriwacki, R.W., Monitoring ligand-induced protein ordering in drug discovery, *Journal of Molecular Biology* (2016), doi: [10.1016/j.jmb.2016.01.016](https://doi.org/10.1016/j.jmb.2016.01.016)

This is a PDF file of an unedited manuscript that has been accepted for publication. As a service to our customers we are providing this early version of the manuscript. The manuscript will undergo copyediting, typesetting, and review of the resulting proof before it is published in its final form. Please note that during the production process errors may be discovered which could affect the content, and all legal disclaimers that apply to the journal pertain.

Monitoring ligand-induced protein ordering in drug discovery

Christy R Grace^{1,5}, David Ban^{1,5}, Jaeki Min², Anand Mayasundari², Lie Min¹, Kristin E Finch^{2,3}, Lyra Griffiths³, Nagakumar Bharatham¹, Donald Bashford¹, R. Kiplin Guy², Michael A. Dyer³, Richard W. Kriwacki^{1,4,*}

¹Department of Structural Biology, St. Jude Children's Research Hospital, 262 Danny Thomas Place, Memphis TN 38105

²Department of Chemical Biology and Therapeutics, St. Jude Children's Research Hospital, 262 Danny Thomas Place, Memphis TN 38105

³Department of Developmental Neurobiology, St. Jude Children's Research Hospital, 262 Danny Thomas Place, Memphis TN 38105; Howard Hughes Medical Institute, St. Jude Children's Research Hospital, 262 Danny Thomas Place, Memphis TN 38105

⁴Department of Microbiology, Immunology and Biochemistry, University of Tennessee Health Sciences Center, Memphis, TN 38105

⁵These authors contributed equally.

*To whom correspondence should be addressed.

Richard Kriwacki

Tel: +001 901 595 3290, FAX: +001 901 595 3032; E-mail: richard.kriwacki@stjude.org

Keywords:

Nuclear Magnetic Resonance; MdmX; Drug Discovery; p53; Nutlin

Abstract

While the gene for p53 is mutated in many human cancers causing loss of function, many others maintain a wild-type gene but exhibit reduced p53 tumor suppressor activity through overexpression of the negative regulators, Mdm2 and/or MdmX. For the latter mechanism of loss of function, the activity of endogenous p53 can be restored through inhibition of Mdm2 or MdmX with small molecules. We previously reported a series of compounds based upon the Nutlin-3 chemical scaffold that bind to both MdmX and Mdm2¹. Here we present the first solution structures based on data from NMR spectroscopy for MdmX in complex with four of these compounds and compare them with the MdmX:p53 complex. A p53-derived peptide binds with high affinity (K_d value of 150 nM) and causes the formation of an extensive network of hydrogen bonds within MdmX; this constitutes the induction of order within MdmX through ligand binding. In contrast, the compounds bind more weakly (K_d values from 600 nM to 12 μ M) and induce an incomplete hydrogen bond network within MdmX. Despite relatively weak binding, the four compounds activated p53 and induced p21^{Cip1} expression in retinoblastoma cell lines that overexpress MdmX, suggesting that they specifically target MdmX and/or Mdm2. Our results document structure-activity relationships for lead-like small molecules targeting MdmX and suggest a strategy for their further optimization in the future by using NMR spectroscopy to monitor small molecule-induced protein order as manifested through hydrogen bond formation.

Introduction

p53 tumor suppression function is lost in the majority of human cancers either through mutation or other inactivation mechanisms². One common inactivation mechanism involves up-regulation of p53 degradation through the ubiquitination pathway. Specifically, overexpression of either Mdm2, a E3 ubiquitin ligase that targets p53, or MdmX, a non-catalytic accessory factor for Mdm2, leads to p53 protein loss and is associated with a wide variety of human cancers. Mdm2 and MdmX each display a conserved N-terminal domain that binds directly to a short linear motif that overlaps with the first transactivation domain (TAD1) within the disordered N-terminal domain of p53. Disruption of the p53:MdmX/Mdm2 interaction through mutation, or inhibition by small molecules, stabilizes and activates p53 through reduced ubiquitination and 26S proteasomal degradation^{3,4}. The Mdm2:p53-TAD1 interaction has been the target of drug discovery efforts for more than a decade and compounds with low nM binding constants for the Mdm2 pocket are in clinical trials against a variety of human cancers, some of which are characterized by Mdm2 overexpression². While less prevalent than Mdm2 overexpression, MdmX is overexpressed in a variety of human cancers², including retinoblastoma³ (>70% of pediatric retinoblastoma cases display MdmX overexpression). However, compounds developed to inhibit Mdm2:p53-TAD1 interactions display relatively low affinity for MdmX⁵. For example, the K_i value for Nutlin-3a toward MdmX is 9.4 μM while that for Mdm2 is 0.06 μM ⁵. Despite relatively low affinity for MdmX, Nutlin-3a, when used at high concentration, was shown to inhibit MdmX:p53 interactions in retinoblastoma cell lines and to stabilize and activate p53³. Furthermore, Nutlin-3a caused regression of retinoblastoma tumors in a mouse model

system. In an effort to improve treatment of retinoblastoma, we have developed a series of improved MdmX inhibitors based upon the Nutlin-3 scaffold¹. Here we report the solution structures based on data from NMR spectroscopy for four of these improved compounds bound to MdmX. The solution structure of the MdmX:p53-TAD1 complex was also determined, allowing comparison with the MdmX:small molecule complexes. These structural data revealed that MdmX, which exhibits conformational exchange in the apo state, becomes more highly ordered upon binding of p53-TAD1, as evidenced by the formation of an extensive network of hydrogen bonds within MdmX. In contrast, the four compounds, which bound more weakly than p53-TAD1, induced fewer hydrogen bonds in MdmX, in particular within a region that is engaged by leucine 22 (L22) of p53-TAD1. Despite their reduced affinity for MdmX in comparison with p53-TAD1, the four compounds did activate p53 in retinoblastoma cell lines. These results suggest a strategy for modifying our current compounds in the future for enhanced interactions with MdmX. NMR spectroscopy will be an invaluable tool for studying the induction of order within MdmX, as monitored by hydrogen bond formation in solution and in our efforts to develop improved MdmX inhibitors for use in retinoblastoma and other cancers that overexpress MdmX.

Results

A novel series of cis-imidazoline compounds bind MdmX and displace p53

A novel series of cis-imidazoline compounds related to the potent Mdm2 inhibitor, Nutlin-3a, was recently synthesized and tested for inhibition of the p53/Mdm2 interaction

using a fluorescence polarization (FP) assay¹. These compounds displayed IC₅₀ values for inhibition of p53 binding to Mdm2 ranging from 0.5 μ M to 3.3 μ M. The IC₅₀ value for Nutlin-3a in the same assay was 0.3 μ M. We adapted this FP assay to monitor inhibition of p53 binding to the MdmX (the N-terminal domain, residues 23-111) and determined IC₅₀ values for a subset of the cis-imidazoline compounds (Figure 1A, Table 1A). Hereafter, we refer to these compounds using the abbreviations given in Figure 1A and Table 1A (SJ057, SJ212, SJ295 and SJ298). The IC₅₀ values for inhibition of the MdmX/p53 interaction ranged from 6.2 to 24.9 μ M and indicated that the compounds bound more weakly to MdmX than to Mdm2. However, the corresponding IC₅₀ value for Nutlin-3a was 18.4 μ M, which indicated that the new cis-imidazoline analogs were more potent inhibitors of the MdmX/p53 interaction than the parent compound, Nutlin-3a.

To understand the thermodynamic basis for the improved potency of the SJ compounds as inhibitors of p53 binding to MdmX, we used isothermal titration calorimetry (ITC) to monitor their binding to MdmX (Figure 1A; Table 1B). As a point of reference, however, we first used ITC to study a peptide corresponding to transactivation domain 1 (TAD1) of p53 (residues 15-29 of human p53, N-S₁₅QETFSDLWKLLPEN₂₉-C; p53-TAD1) binding to MdmX. The equilibrium dissociation constant (K_d^{ITC}) for p53-TAD1 binding to MdmX was 0.15 ± 0.04 μ M (Table 1B), in agreement with a previous report⁶. This interaction was enthalpically driven (Table 1B; $\Delta H = -17.5 \pm 0.3$ kcal mol⁻¹) and was accompanied by a large entropic penalty ($-T\Delta S = +8.1 \pm 0.1$ kcal mol⁻¹), probably due, at least in part, to folding of the disordered p53-TAD1 peptide upon binding to MdmX. We next analyzed the binding of three of the SJ compounds to MdmX using ITC (Figure 1B-E, Table 1B). While the IC₅₀ and K_d^{ITC}

values for SJ295 and SJ298, respectively, were similar, these values were different for SJ057, with ITC indicating a sub-1 μM K_d^{ITC} value. The thermodynamic driving force for binding of the small molecules to MdmX varied, with the binding reaction being primarily enthalpically driven for SJ295 and SJ298 and both enthalpically and entropically driven for SJ057 (Table 1B). ITC data could not be recorded for SJ212 due to aggregation at high concentration (see Supplemental Experimental Procedures). To overcome the limitations associated with ITC analysis of SJ212, and to confirm binding results for the other SJ compounds, we next employed NMR spectroscopy, which is well-suited for studies of small molecule/protein interactions with K_d values in the low μM range⁷.

The two-dimensional (2D) [^{15}N , ^1H] HSQC spectrum of apo MdmX (Figure 2A, black contours in all panels) is consistent with a folded, globular protein domain and with a past report⁸, although a resonance peak was not observed for all residues (discussed below). The binding of p53-TAD1 and the four SJ compounds to MdmX was analyzed by monitoring chemical shift perturbations (CSPs) during titration experiments (Figure 2B and Figure S1A). p53-TAD1 bound tightly in the slow exchange regime and, therefore, a K_d value for binding to MdmX could not be determined. However, the SJ compounds bound in the fast exchange regime and multi-point titrations (Figure S1A) allowed binding curves to be generated, curve fitting to a two-site binding model to be performed (Figure 2C), and K_d values to be determined (K_d^{NMR} ; Figure S1B and Table 1C). The K_d values for these small molecule/MdmX interactions, between 0.6 and 6 μM , were at the lower limit for quantitative analysis using NMR^{9,10}; therefore, we utilized a unique approach and conservative error analysis to determine the K_d^{NMR} values (see Supplemental Experimental Procedures). The K_D^{NMR} values for SJ295, SJ298, and

SJ057 were in agreement with those determined by ITC (Table 1B) and that for SJ212 was able to be determined ($K_D^{\text{NMR}} = 0.6 \pm 0.6 \mu\text{M}$). Thus, analysis by ITC and NMR afforded consistent K_d values for the cis-imidazoline compounds binding to MdmX, with SJ057 and SJ212 exhibiting the highest affinity. To investigate the structural basis for the different affinities of p53-TAD1 and the SJ compounds for MdmX, we next determined the structures of the individual complexes using NMR spectroscopy.

Structural analysis of MdmX:ligand complexes; complexes with p53 and SJ cis-imidazoline compounds

The ligand binding-induced changes in NMR chemical shift values obtained through the titration experiments discussed above provided a basis for qualitatively comparing the solution structure of MdmX when bound to p53 and the SJ cis-imidazoline compounds (Figure S2). Three aromatic and hydrophobic residues within p53-TAD1 have previously been identified as being critical for binding to MdmX, including phenylalanine 19 (F19), tryptophan 23 (W23) and leucine 26 (L26)^{6,11}. These residues bind deeply within pockets (termed the “F19 pocket”, “W23 pocket”, and “L26 pocket”⁶) on the surface of MdmX and therefore influence NMR chemical shift values of nearby residues, providing a “fingerprint” of the solution structure of MdmX bound to p53-TAD1. Strikingly, the patterns of chemical shift perturbations (CSPs; relative to the chemical shift values of apo MdmX) caused by the binding of p53 and the four SJ compounds to MdmX were very similar, with the largest perturbations observed for residues within α -helices 2 and 4 ($\alpha 2$, $\alpha 4$), N-terminal residues and β -strand 3 ($\beta 3$), and loops 2 and 3 ($L2$, $L3$; Figure S2). However, some of the perturbations caused by

binding of p53 (Figure S2B) were not recapitulated by binding of the small molecules, in particular those for $\beta 2$ and $L3$ (Figure S2B-F), suggesting that the small molecules engage MdmX in these regions differently than p53-TAD1. To understand the similarities and differences between the various MdmX:ligand complexes in greater detail, we next pursued structure determination of the various MdmX:ligand complexes at atomic resolution.

We initially pursued structure determination of apo MdmX and its complexes with the SJ compounds using X-ray crystallography but were unable to obtain suitable crystals for any of the samples. Therefore, we pursued structure determination of these complexes as well as that with p53-TAD1 in solution using NMR spectroscopy. Initially, we studied apo MdmX, but, in the absence of a ligand, this protein exhibited only ~70% of the expected backbone amide resonances in the 2D [^{15}N , ^1H] HSQC spectrum (Figure S3A) and was unstable in solution, precluding structure determination. Assignment of the visible resonances revealed that most of the invisible resonances corresponded to residues in $L2$ and $L3$ between $\alpha 2$ and $\alpha 3$, $\alpha 3$ and $\alpha 4$, respectively (Figure S2), suggesting that this region, in the absence of a ligand, experiences conformational exchange most likely between the intermediate to fast exchange regimes. However, for residues in apo MdmX that could be assigned, an analysis of $^{13}\text{C}\alpha$ chemical shift values indicated that apo MdmX exhibited four α -helices (Figure S3B), consistent with the secondary structure of MdmX bound to p53-TAD1 determined previously using X-ray crystallography⁶ (Figure S3B). Furthermore, the observation of well dispersed resonances in the 2D HSQC spectrum suggested a globular structure for the observable residues in apo MdmX.

Because structure determination of MdmX bound to the SJ compounds was only possible using NMR spectroscopy, we began our comparative structural analyses by determining the structure of p53-TAD1 bound to MdmX in solution using NMR (Figure 2A). Standard NMR methods were used to assign backbone and sidechain resonances, and distance restraints were collected using conventional techniques (see Methods). The secondary structure of MdmX within the complex with p53-TAD1 in solution (based upon analysis of $^{13}\text{C}_\alpha$ chemical shift values) was very similar to that observed in the crystal structure (Figure S3B). Furthermore, the 3D structures determined in solution (Figure 3A, Table 2) and in crystals (PDB: 3DAB) were very similar [backbone heavy atom root mean squared deviation (RMSD), 0.99 Å]. The p53-TAD1 peptide adopted an α -helical conformation between residues F19 and L26, as previously observed^{6,12}. The patterns of ^1H - ^1H nuclear Overhauser effects (NOEs) for residues 15-18 and 27-29 (data not shown) indicated that these N- and C-terminal regions, respectively, of p53-TAD1 were disordered. In contrast, intermolecular ^1H - ^1H NOEs were observed from the side chains of F19, L22, W23, and L26 of p53-TAD1 to methionine 53 (M53), leucine 56 (L56), glycine 57 (G57), isoleucine 60 (I60), valine 74 (V74), valine 92 (V92), and leucine (L98) of MdmX (Figure S4A), which allowed structure determination and confirmed the role of hydrophobic interactions in the formation of the MdmX:p53-TAD1 complex¹².

Among the four compounds, analysis by ITC showed that SJ295 and SJ298 exhibited the lowest binding affinity for MdmX (K_d^{ITC} values of 4.7 μM and 12.0 μM , respectively), while SJ057 exhibited the highest affinity (0.6 μM) (Figure 1; Table1B). SJ212 was shown by NMR to also bind with high affinity to MdmX (K_d^{NMR} value of 0.6

μM ; Table 1C). We used standard NMR methods to assign backbone and sidechain resonances for all of the residues of MdmX bound to the four SJ compounds at a 1:1 molar ratio (2D [^{15}N , ^1H] HSQC spectra are illustrated in Figure 2A). (Note that the backbone amide resonance for V92 of MdmX bound to SJ295 could not be assigned.) The overall trend in $^{13}\text{C}_\alpha$ and $^{13}\text{C}_\beta$ chemical shifts [quantified as $(\delta^{13}\text{C}_\alpha - \delta^{13}\text{C}_\beta)$, $\Delta\delta^{13}\text{C}_{\alpha/\beta}$] observed for the four MdmX:SJ complexes were very similar (Figure S3C). However, differences between $\Delta\delta^{13}\text{C}_{\alpha/\beta}$ values for the four MdmX:SJ complexes and MdmX:p53-TAD1 (Figure S3B) were observed for residues at the end of the $\alpha 2$ helix and in L2 and L3 (Figure S3D). Analysis of three-dimensional (3D) ^{13}C - and ^{15}N -edited NOESY spectra provided numerous intra-molecular distance restraints for structure determination of MdmX bound to each of the SJ compounds (see Supplementary Methods for details of structure determination).

Resonances of the MdmX-bound SJ compounds were assigned through the analysis of 2D [^{13}C , ^{15}N]-filtered TOCSY and NOESY spectra (Table S1) and inter-molecular NOEs between MdmX and the SJ compounds were measured using 2D ^{13}C -, or ^{15}N -edited half-filtered NOESY experiments (Figure S4D). Protons of all four of the compounds exhibited NOEs to those of residues within the hydrophobic groove of MdmX (including M53, L56, I60, V74, V92, and L98; Figure S4D), which are the same residues contacted by the key hydrophobic residues of p53-TAD1 (F19, W23 and L26; Figure S4A, D). However, the inter-molecular ^1H - ^1H NOEs were generally of lower intensity for the complexes with the SJ compounds *versus* that with p53-TAD1, suggesting that some of the small molecules do not bind as deeply within the hydrophobic groove of MdmX as does the p53 peptide. Our solution structures (Figure

3, Table 2) showed that the para-chloro-phenyl group of the SJ compounds bound within the pocket on MdmX that was occupied by W23 of p53-TAD1 (the “W23 pocket”) and that the adjacent substituent on the 4 position of the diazole ring (e.g., meta-chloro-phenyl in SJ295) bound within the “L26 pocket”¹³ (Figure 3). The substituents at this position in the different SJ compounds exhibited different patterns of inter-molecular NOEs but, in all cases, the numbers of NOEs were sufficient to uniquely position these moieties within the L26 pocket of MdmX. The complete analysis, example spectra comparing the ¹H-¹H intermolecular NOEs, and the intermolecular NOEs plotted onto the complex structures can be found in Figure S4. The substituent at the 2 position of the diazole ring bound within an additional but more shallow pocket on MdmX that, with p53-TAD1, was occupied by F19 (the “F19 pocket”). Protons within the piperazine moiety, which enhances the aqueous solubility of the compounds, did not display inter-molecular NOEs due to being completely solvent exposed in the complexes. The solution structures of the various MdmX:SJ compound complexes are well-defined by intra- and inter-molecular distance and other structural restraints (Figure 3, Table 2), as evidenced by low backbone atom RMSD values for the individual ensembles (backbone atom RMSD values < 0.5 Å; Table 2), zero distance restraint violations and acceptable Ramachandran backbone torsion angle statistics (Table 2). Furthermore, we have compared the backbone and heavy atom RMSDs between all MdmX complexes presented here (Table S3). The RMSD for the backbone of the complexes ranges from 0.7 to 1.5 Å suggesting that the overall fold of MdmX upon compound binding is very similar to that of p53-TAD1, although there are subtle differences in the conformations in the *L1*, $\alpha1$ and $\alpha3$ regions. In the following sections, we discuss the features of the

complexes of MdmX with p53-TAD1 and the SJ compounds and the insights they provide into structure-activity relationships.

Comparison of the MdmX binding modes for the SJ compounds and the p53-TAD1 peptide

We compared the solution structures of the various MdmX:ligand complexes to understand the extent to which the SJ compounds mimic the inter-molecular interactions observed with the MdmX:p53-TAD1 complex. As previously observed in crystals, the solution structure with p53-TAD1 showed that the side chains of F19, W23 and L26 (of p53) were deeply buried within the hydrophobic groove of MdmX (Figure 3A). In addition, the side chain of L22 within p53-TAD1 interacted with MdmX. We term these four residues the MdmX-binding “pharmacophore” of p53-TAD1. The conformations of these residues within the MdmX:p53-TAD1 complex were very similar in crystals (PDB 3DAB) and in solution (reported here; Figure 4A). As has been previously discussed⁶, three of these residues bind into distinct “pockets” on MdmX. We additionally include L22 in the p53-TAD1 pharmacophore because two of the SJ compounds (SJ212 and SJ298, Figure 4C and 4D) more closely engage a region within the hydrophobic pocket of MdmX that is also engaged by the side chain of L22. Specifically, the meta-methoxy-phenyl rings of SJ298 and SJ212, in addition to occupying the L22 pocket, also engage residues within *L3*; the side chain of L22 within p53-TAD1 also engages residues within *L3* (Figure 3). These SJ compound:MdmX interactions, which alter the conformation of *L3*, are absent in the complexes of MdmX with SJ295 and SJ057. In addition to our observations, several studies have shown that

the side chain of L22 contributes to the binding of p53 to both Mdm2 and MdmX. Specifically, through hydrophobic interactions, L22 facilitates additional electrostatic and water-mediated hydrogen bonds within MdmX that are favorable for binding¹⁴⁻¹⁶. Therefore, we include L22, in addition to F19, W23 and L26, in the p53-TAD1 pharmacophore.

We next used this pharmacophore as a basis for comparing the structures of the four SJ compound:MdmX complexes. While each of the SJ compounds place chemical moieties in positions that overlap with several residues of the p53-TAD1 pharmacophore, some features of the various complexes with MdmX are different (Figure 4). We analyzed two general features of these complexes to illustrate these differences. First, we analyzed the extent of overlap of chemical moieties of the SJ compounds with F19, W23, and L26 of the p53-TAD1 pharmacophore. The compounds SJ295, SJ212 and SJ057 position chemical moieties that overlap well with F19, W23 and L26 of the p53-TAD1 pharmacophore but SJ298 only positions moieties that overlap well with F19 and W23 and not with L26 (Figure 4). The meta-methoxy-phenyl moiety on the 4 position of the diazole ring of SJ298 projects deep into the hydrophobic pocket of MdmX, away from the region occupied by L26 of the p53-TAD1 pharmacophore whereas the other compounds occupy this region. In addition, the isopropyl-oxy moiety of SJ298 engages a slightly different region of the F19 pocket of MdmX in comparison with the other three SJ compounds (Figure 4). The projection of SJ298 more deeply within the hydrophobic pocket of MdmX, in comparison with the other compounds, may explain why many more intermolecular NOEs were observed with the MdmX: SJ298 complex than with the others (Figure S4 and Table 2). However,

this compound bound more weakly than the other compounds which penetrate less deeply into the hydrophobic pocket of MdmX. The depth at which SJ298 sits in the binding pocket highlights MdmX's plasticity. Second, we compared how the SJ compounds engage the L22 pocket. The para-methoxy moieties of both SJ212 (Figure 4C) and SJ298 (Figure 4D) occupy this region of MdmX. However, while SJ295 exhibits the same phenyl ring substituent, a different alignment of the phenyl ring causes this moiety to project upwards towards L2 and solvent rather than toward the L22 pocket (Figure 3B, Figure 4B). Interestingly, SJ057 exhibits a para-cyano moiety in place of the para-methoxy of the other compounds, and this moiety also projects upwards toward L2 within MdmX and solvent (Figure 3), but this substituent is associated with the highest affinity for MdmX (Table 1). These structural observations did not provide a rationale for the differences in the MdmX binding affinities of the SJ compounds. Therefore, we next examined other experimental differences between the various MdmX:ligand complexes. Specifically, we sought explanations for differences in the effects of the association of p53-TAD1 *versus* the SJ compounds on the NMR chemical shift values of MdmX. While the binding-induced CSPs associated with the different ligands were generally similar, notable differences were observed (Figs. S2 & S3). These issues are discussed below.

Differences in hydrogen-bonding within MdmX in its complexes with SJ compounds and p53-TAD1

Although the structures of MdmX within its complexes with SJ compounds were very similar to that with p53-TAD1, 2D ^1H - ^{15}N HSQC spectra for MdmX within the small

molecule and p53-TAD1 complexes revealed notable differences (indicated by black boxes in Figure 2A). In particular, the backbone amide resonances for H72 and V92 (Figure S5A), exhibited dramatically different chemical shift values [e.g., large chemical shift differences when MdmX was bound to p53-TAD1 *versus* the SJ compounds (CSDs = $\Delta\delta^{\text{MdmX:p53-TAD1}} - \Delta\delta^{\text{MdmX:SJ-complex}}$; Figure 5A]. These CSDs were determined under conditions where the complexes were fully bound. The resonances of other residues flanking those noted above also exhibited CSDs in the two types of complexes (including from M53 to L56, from I60 to Y66, H72 & M73, from V92 to Y99, and R103; Figure 5A and Figure S5B). These residues that showed large CSDs within the MdmX:SJ057 complex also exhibited CSDs in the other MdmX:SJ compound complexes (Figure S5B). The observation of extensive CSDs between the two types of complexes, with some of these residues exhibiting CSDs distant from the p53-TAD1 binding groove within MdmX (Figure S2), suggested that differences between the two types of complexes extend beyond the inter-molecular interfaces. However, because the 3D structural features of MdmX within the different complexes were similar (Table 2 and S2), other physical differences, not revealed by time-averaged atomic coordinates, are likely to be responsible for the large chemical shift differences. between their spectra. In the next section, we discuss the possible origins of these spectral differences by comparing the features of MdmX bound to SJ057, the SJ compound that exhibits the highest affinity for MdmX (Table 1), with those for the complex with p53-TAD1. Importantly, our observations for the complex with SJ057 are recapitulated for the complexes with the other SJ compounds (Figure S5-S6).

Chemical shift values of backbone nuclei report on polypeptide backbone structure¹⁷ and dynamics¹⁸ and are influenced by several factors, including backbone/sidechain conformation, aromatic ring currents, fluctuating electric fields, magnetic anisotropy, and hydrogen bonding^{19,20}. Therefore, we evaluated the possible contributions from some factors that may give rise to the large CSDs observed for amide proton ($^1\text{H}_\text{N}$), amide nitrogen (^{15}N), and carbonyl carbon ($^{13}\text{C}'$) nuclei of MdmX when bound to SJ057 *versus* p53-TAD1 (Figure 5A). We can rule out large conformational differences between the two complexes as a source of the large CSDs because the structures of MdmX when bound to these two ligands, as previously discussed, were very similar (backbone heavy atom coordinate RMSD, ~ 1 Å; Figure 3, Figure S3B-C, Table 2). The p53-TAD1 peptide contains several aromatic amino acids and SJ057 also contains several aromatic moieties; therefore, differences in the orientation of aromatic rings for the two types of ligands when bound to MdmX could possibly contribute to the noted CSDs in the form of ring current effects, especially for $^1\text{H}_\text{N}$ resonances. Using our 3D solution structures, we calculated the ring current²¹ and electric field contributions²² to MdmX chemical shifts for its complexes with the five ligands studied here; however, these effects alone could not account for the large observed CSDs (Figure S5B), especially for residues H72 and V92, which exhibited the largest CSDs. Therefore, we next considered differences in hydrogen bonding within MdmX when bound to p53-TAD1 and SJ057 as a factor contributing to the large NMR CSDs.

We quantitatively analyzed the networks of backbone hydrogen bonds (H-bonds) observed within MdmX for each of the five ligand complexes. For this analysis, we

generated *de novo* structures for each of the complexes that utilized only ^1H - ^1H distance restraints derived from ^1H - ^1H NOE values, without H-bond restraints (statistics for these structures are provided in Table S2). This was feasible due to the large number of distance restraints determined for the MdmX:ligand complexes discussed herein (Table S2). This protocol avoided bias in the 3D structures associated with the introduction of explicit backbone H-bond restraints, as was done for the final structures (see Methods). We note, however, that the final structures that were deposited (Table 2) exhibit improved Ramachandran statistics compared to the structures in which the H-bonds were removed and that were used for the following analysis. The numbers and energies of backbone H-bonds for each of the 20 lowest-energy structures for each of the five MdmX:ligand complexes were determined using established procedures²³⁻²⁵. We emphasize that these energies are calculated based on geometrical factors using a parameterized energy function and only serve as a quantitative metric to reveal differences amongst MdmX complexes but are not otherwise interpretable as true energies. The MdmX:p53-TAD1 complex exhibited a mean of 34 H-bonds per structure within the NMR bundle (with the minimum (maximum) H-bond per structure being 29 (39)), with a mean energy of $7,333 \pm 10$ A.U. per H-bond (mean \pm standard error of the mean; A.U., arbitrary energy units; Figure 5B). [Note that favorable energies are positive] For the MdmX:SJ057 complex, there were a mean of 30 H-bonds per structure (with the minimum (maximum) H-bond per structure being 27 (33)), with a mean energy of $7,310 \pm 12$ A.U. per H-bond (solid black lines; Figure 5B and S6A). Therefore, the complex of MdmX: with p53-TAD1 exhibited a larger number of H-bonds, with slightly larger energies, than the MdmX:SJ057 complex. Furthermore, the total H-bond energy

(sum over all average H-bond energies) was 17% larger for the p53-TAD1 complex than the SJ057 complex. The average standard error in H-bond energy over all residues was similar for the structures (Figure 5C; $\langle\sigma_{E-HB}\rangle = 10.3$ A.U. for MdmX:p53-TAD1 and $\langle\sigma_{E-HB}\rangle = 10.8$ A.U. for MdmX:SJ057), but was generally larger in value for all SJ compound complexes than for the p53-TAD1 complex. Importantly, there were 12 H-bonds that occurred at least once in the MdmX:p53-TAD1 complex that *never* occurred in the complex with SJ057 (Fig. 5C, negative gold bars). These changes in the number of H-bonds, unlike the small variations between the ones that were observed in both the p53-TAD1 and the small molecule complex (Fig. 5B, C and Fig. S6B), are the primary focus of this analysis. Interestingly, there were four H-bonds that occurred only in the MdmX:SJ057 complex (Fig. 5C, negative black bars). The H-bonds that occurred exclusively when p53-TAD1 was the ligand were clustered in two regions of MdmX, including residues within $L2-\beta2$, $\beta3-L3$, and the N- and C-termini (Figure 5C, 5D). Many of the residues of MdmX that exhibited CSDs when bound to the two ligands are within regions lacking H-bonds in the MdmX:SJ057 complex (Figure 5D; green shaded region), including those within the $L2-\beta2$ and $\beta3-L3$ regions as well as nearby $\alpha2$ (which, however, did not exhibit H-bond differences). The H-bond differences for residues within the N- and C-termini, which exhibited small CSDs between the two structures, arose because some structures within the ensemble for the MdmX:p53-TAD1 complex exhibited a short β -strand between these segments. These results suggest that, in addition to the other factors discussed above (Figure S5), differences in patterns of H-bonds within MdmX when bound to p53-TAD1 versus SJ057 contribute to the observed

CSDs between the two complexes. Similar H-bond differentials were observed between the MdmX:p53-TAD1 complex and the other three MdmX:SJ complexes (Figure S6).

Discussion

Small molecules based on the Nutlin-3a scaffold designed to mimic the p53 pharmacophore are classically defined to include residues Phe19, Trp23, and Leu26. These Nutlin-3a-based molecules generally exhibit higher binding affinity for Mdm2 than MdmX, although the p53-TAD1 peptide displays similar affinity for Mdm2 and MdmX [(K_d values of 0.24²⁶ and 0.15 μM (Table 1B), respectively] and the structures of these two proteins when bound to the p53 peptide are similar^{4,5}. Thus, while p53-TAD1 binds in a structurally similar manner, with similar affinity, to Mdm2 and MdmX, previously reported Nutlin-3a-like molecules exhibit different binding affinities for these two p53 regulatory proteins. The molecules discussed herein show improved binding to MdmX (in comparison with Nutlin-3a) and maintain moderate affinity for Mdm2. Further, the SJ compounds show promise as inhibitors of p53 degradation in cancer cells that overexpress MdmX. We observed that the SJ compounds induced expression of the p53-dependent cell cycle inhibitor p21^{Cip1} (p21) in two retinoblastoma cell lines known to overexpress MdmX (Weri1 and Y79 cells)³ (Figure 6A). In particular, SJ057, the compound that bound most tightly to MdmX in NMR and ITC binding assays (Table 1), activated p21 expression in these two cell lines to the same extent as Nutlin-3a. Nutlin-3a, which binds with high affinity to Mdm2 and low affinity to MdmX, probably acts in this assay by disrupting Mdm2/p53 interactions. In contrast, SJ057 may inhibit

interactions between p53 and both Mdm2 and MdmX to activate p21 expression.

Currently, our data does not allow us to ascribe activation of p21 expression to specific interactions with either Mdm2 or MdmX. However, the SJ compounds do bind to MdmX more tightly than does Nutlin-3a, suggesting that their ability to activate p21 may, at least in part, be due to their inhibition of MdmX:p53-TAD1 interactions. Furthermore, the observed SJ compound-dependent activation of p21 expression was shown to be p53 dependent using $p53^{+/+}$ and $p53^{-/-}$ HCT116 cells (Figure 6B). These preliminary cellular findings provide motivation to apply the knowledge on structure-activity relationships for the SJ compounds gained through the current studies to design improved MdmX inhibitors in the future.

Our structural results suggest that small molecule ligands of MdmX should, in addition to occupying the F19, W23 and L26 pockets on MdmX, mimic the interaction of L22 of p53 with the *L2*, $\beta 2$, $\beta 3$, and *L3* region of MdmX (Figure 3 & Figure 4). In the solution structure of MdmX with p53-TAD1, this interaction is associated with an extensive network of H-bonds and distinctive NMR chemical shift values for residues within this β -strand and loop-containing region (Figure 5). Two of the SJ compounds, SJ212 and SJ298, position a methoxy group near the L22 pocket of MdmX, but this substituent is less bulky than the side chain of L22 in p53 and probably incompletely engages residues within the *L2*, $\beta 2$, $\beta 3$, and *L3* region. For the two other SJ compounds, SJ295 and SJ057, the para benzyl substituents (methoxy and cyano, respectively) project away from the L22 pocket (Figure 4). However, other moieties in SJ057 do interact with the *L2* region, leading to a conformation similar to that observed in the complex with p53-TAD1 (Figure 3). We note that there is roughly a ten-fold

difference between the affinities for the two compound pairs, SJ057/SJ212 and SJ295/SJ298. Comparison of the four NMR-derived ensembles indicates that these thermodynamic differences are not due to clear differences between the two pairs of structures. However, we suggest that the thermodynamic differences are due to differences in the H-bond patterns between the different MdmX:small molecule complexes (Figure 5 and Figure S6). The 2D ^1H - ^{15}N HSQC spectrum of apo MdmX, lacking resonances for ~30% of the backbone amide groups, provides evidence that, in the absence of a ligand, this protein exhibits dynamics on the intermediate to fast NMR timescales (Figure S3A). Interestingly, most of the missing resonances correspond to residues within the *L2*, $\beta 2$, $\beta 3$, and *L3* region of MdmX. This is in contrast to the closely related apo Mdm2, which exhibits peaks in 2D HSQC spectra for virtually all backbone amide groups²⁷. When p53-TAD1 binds, all of the missing resonances of MdmX appear, indicating that motions of these amide groups are dampened such that they either shift into the slower kinetic exchange regime or depopulate alternative conformations. We propose that future efforts to develop higher affinity MdmX-binding small molecules should be directed toward engaging the L22 pocket so as to dampen intrinsic backbone dynamics and to allow for the formation H-bonds within the β -strands and loops in this region of MdmX. The chemical shift values for the amide groups of H72 and V92, while partially influenced by aromatic ring current effects (Figure S5B), could serve as reporters of H-bond formation within this region of MdmX. Solution NMR spectroscopy is a powerful tool in further optimization of small molecule inhibitors of MdmX, through simple 2D HSQC analysis to monitor spectra parameters related to H-bond formation and also through 3D structure determination and the analysis of H-bond

networks within MdmX. Furthermore, in the future, NMR can be used to reveal the role of protein dynamics, and changes in protein dynamics upon ligand binding, in the differential affinity of MdmX for p53 *versus* the SJ compounds. An initial survey of the ^{15}N backbone dynamics for the MdmX:p53-TAD1, MdmX:SJ057, and MdmX:SJ298 complexes indicated that the energy landscape for MdmX is multistate and highly variable depending on the small molecule bound to MdmX (Figure S7). Our initial results indicate that fast, pico-nanosecond motions are not variant, but future concentration-dependent relaxation dispersion experiments will be necessary to understand the dynamic differences amongst MdmX:ligand complexes.

The ITC data showed that the MdmX:p53-TAD1 interaction was entropically unfavorable ($-T\Delta S = 8.1 \text{ kcal mol}^{-1}$) and that this was counter-balanced by a highly favorable enthalpy of binding ($\Delta H = -17.5 \pm 0.3 \text{ kcal mol}^{-1}$; Table 1B). The binding of the SJ compounds (except SJ212, which could not be analyzed) to MdmX generated different thermodynamic profiles, with SJ295 and SJ057 exhibiting a balance between favorable enthalpic and entropic terms and SJ298 exhibiting a dominant, favorable enthalpic term counter-balanced by a small, unfavorable entropic term (Table 1B). It is well established that the binding of disordered polypeptides such as p53-TAD1 to folded binding partners is accompanied by an entropic penalty due to folding upon binding^{26,28,29} and this phenomenon accounts, at least in part, for the large entropic penalty for p53-TAD1 binding to MdmX. In addition, as discussed above, dynamics within MdmX are dampened upon p53-TAD1 binding, possibly giving rise to an additional unfavorable entropic contribution. The binding of all of the SJ compounds to MdmX is associated with the observation of NMR peaks for amide groups that are

missing for apo MdmX, indicating that these ligands also dampen dynamics within MdmX upon binding. Support for ordering of the *L2*, $\beta 2$, $\beta 3$, and *L3* region as a factor contributing to the entropic penalty associated with p53-TAD1 binding to MdmX is provided by thermodynamic data for this ligand binding to Mdm2³⁰. In this case, the entropic penalty for p53-TAD1 binding to Mdm2, $-T\Delta S = +2.2\text{-}2.6 \text{ kcal mol}^{-1}$ ³⁰, was much smaller than the value reported herein for binding to MdmX ($+8.1 \pm 0.1 \text{ kcal mol}^{-1}$; Table 1B). The small entropic penalty associated with binding to Mdm2 probably arises because the *L2*, $\beta 2$, $\beta 3$, and *L3* region of Mdm2 is mostly ordered prior to binding²⁷. We suggest that the network of hydrogen bonds promoted in MdmX due to binding of p53-TAD1 contributes to the large and favorable ΔH of binding that overcomes the accompanying substantial entropic penalty. ITC and NMR should be used in the future to monitor the induction of order within the *L2*, $\beta 2$, $\beta 3$, and *L3* region of MdmX, and the extent of this rigidification can be used as a criterion for optimization of small molecule ligands of MdmX. Small molecules that fully engage the L22 pocket of MdmX may afford more extensive rigidification of this region in MdmX, but should also capture the large favorable entropic contribution as observed for SJ057. Further compound optimization would benefit by applying strategies established by Frieri and co-workers³¹ which involves capturing and maintaining enthalpically favorable interactions at small molecule:protein interfaces through chemical modification of the small molecule.

Conclusion

We present the first NMR-derived solution structures for MdmX in complex with p53-TAD1 and four SJ compounds that are based upon the Nutlin-3a scaffold. Residues F19, L22, W23 and L26 of p53-TAD1 bind tightly forming hydrophobic interactions with the pocket of MdmX and these interactions were associated with rigidification and the formation of a H-bond network within regions of MdmX. In contrast, the SJ compounds bound more weakly to MdmX and induced a less extensive network of H-bonds within these regions. NMR chemical shift values for a few key residues within these regions of MdmX were correlated with the extent of binding-induced rigidification for the two types of ligands. Analysis of thermodynamic parameters showed that the binding of p53-TAD1 was associated with a large entropic penalty and that this penalty was smaller for binding to the SJ compounds, consistent with a reduced binding-induced rigidification of MdmX. Our results suggest that combined use of NMR spectroscopy and ITC for the analysis of binding-induced rigidification and H-bond formation will enable the optimization of small molecule ligands for MdmX in the future.

Experimental Procedures

Synthesis of SJ-compounds

All the four SJ compounds were synthesized according to the method reported recently¹.

Protein Expression and Purification

Human MdmX (23-111) was expressed in *E. coli* strain BL-21(DE3) (Novagen). Cells were taken up in a lysis buffer of 25 mM Tris (pH 8.0), 500 mM NaCl and 2 mM TCEP. Affinity purification was initially done by Ni-NTA followed by cleavage of His₆-tag using the TEV protease. A second Ni-NTA purification was performed, followed by size exclusion chromatography using a Superdex 75 preparative column in 25 mM Tris (pH 8.0), 300 mM NaCl, and 2 mM TCEP. Sample purity was confirmed by SDS-PAGE. Isotope labeled protein was grown using a MOPS based minimal media, but purification protocols were the same as described above.

NMR Sample Conditions

MdmX concentrations for the binding affinity titration were between 60-70 μ M, and were performed in a 10 mM sodium phosphate buffer (pH 6.5) with 200 mM NaCl, 2mM TCEP and 0.05% sodium azide solved in 90% H₂O/10% D₂O. Free MdmX assignment experiments were carried out on MdmX at 100 μ M concentration in the same buffer. Structural data were collected on MdmX complexes with SJ compounds or p53 peptide

at 1 mM concentration in the same buffer. All the spectra were collected at 298 K. The binding of all SJ compounds to MdmX was also queried by two dimensional [^{15}N , ^1H]-HSQCs titrations (see supplemental Experimental Procedures). For all experimental details please see the supplemental Experimental Procedures.

ACCESSION NUMBERS

Atomic coordinates for the structures of the complexes, MdmX:p53-TAD1, MdmX:SJ295, MdmX:SJ212, MdmX:SJ057 and MdmX:SJ298 have been deposited in the protein data bank database with following ID codes 2MWY, 2N14, 2N0W, 2N0U and 2N06 respectively. The chemical shifts were deposited in BMRB data base as well and the accession numbers are linked to the pdb server.

AUTHOR CONTRIBUTIONS

C.R.G., D.B., Z.S., A.M., J.M., K.F., L.M., N.B., D.B. performed experiments and analyzed data. C.R.G., D.B., and R.W.K wrote the manuscript with input from all the authors.

ACKNOWLEDGEMENTS

The authors acknowledge Dr. Zhengding Su for expert technical assistance with NMR analysis of small molecule-MdmX interactions in the early stages of this project. This work was supported by a US National Cancer Institute Cancer Center Support grant P30CA21765 (at St. Jude Children's Research Hospital) and ALSAC. D.B. would like to acknowledge support from the NIGMS (F32GM113290).

Figure Legends

Figure 1. SJ compounds bind to MdmX based on ITC

(A) Structures of the p53-TAD1 peptide with targeted pharmacophore residues (F19, W23, and L26) drawn as sticks and all chemical structures for the compounds studied here. Chemical structures of compounds derived from the Nutlin-3a scaffold and functional motifs corresponding to the p53-TAD1 peptide residue it was intended to mimic are boxed for the SJ295 molecule. (B-E) Calorimetric data for MdmX titrations with SJ compounds by ITC collected at 298 K. Titrations of MdmX with (B) p53-TAD1, (C) SJ295, (D) SJ298 and (E) SJ057 are represented above. Observed heats are reported after subtraction of the heats of dilution from the recorded heat series. Integrated heats are fitted and are represented by the solid black line through the isotherm.

Figure 2. SJ Compounds bind to MdmX in the binding pocket of p53-TAD1

(A) Superimposed [^{15}N , ^1H] HSQC spectra of apo MdmX (black contours) and MdmX in complex (1:1 molar ratio) with p53-TAD1 peptide (brown contours), SJ295 (red), SJ212 (blue), SJ298 (green) and SJ057 (gold). A Few amide resonances are marked for clarity that exhibit three different types of behavior upon complex formation. Resonances labeled in black appear in apo as well as the MdmX-complex spectrum. Resonances labeled in color were observed only in the spectrum of MdmX-complex and hence were reassigned. Resonances within grey boxes appear in the same position in MdmX:p53-

TAD1 and MdmX:SJ complexes, while those within black boxes appear at different positions in MdmX:p53-TAD1 and MdmX:SJ complexes and their position in MdmX:p53-TAD1 complex is highlighted in all the spectra. (B) Overlaid [^{15}N , ^1H]-HSQCs displaying Gly82 resonance shown in (A), for all SJ compounds. Increasing concentration of SJ compound is denoted by changes in color from green (free MdmX) to red (saturated MdmX). (C) Characteristic binding isotherms for Gly82 of MdmX from SJ295 (red dots), SJ212 (blue dots), SJ298 (green dots), and SJ057 (gold dots) NMR-based titrations. Solid black lines indicate fitting using only its own K_D for ^{15}N nucleus of Gly82. Dashed lines (red, SJ295; blue, SJ212; gold, SJ057; green, SJ298) correspond to fits when a single K_D was used to describe all nuclei together (global K_D). There is a difference for SJ295 when the global fitting K_D was used. This stems from the heterogeneity in the local K_D s observed for this compound (see Figure S1B).

Figure 3. 3D NMR structures of MdmX complexes

(A) MdmX:p53-TAD1 (brown), (B) MdmX:SJ295 (red), (C) MdmX:SJ212 (blue), (D) MdmX:SJ298 (green) and (E) MdmX:SJ057 (gold). 20 lowest energy structures are shown after superimposing the backbone heavy atoms. Residues 23-26 and 107-111 of MdmX (unstructured) are not displayed for clarity. The lowest energy conformer is displayed in the ribbon representation in the middle panel, showing that the tertiary fold of the complexes are very similar and the compounds bind hydrophobic pocket of p53-TAD1 (lower panel). The lower panel indicates a close view of how the small molecules

sit in the p53-TAD1 binding pocket causing some perturbations through the L2 up to the L3 region. MdmX is shown in surface representation that is colored based on charge.

Figure 4. Difference in the pharmacophore for SJ compounds and p53-TAD1 peptide

Binding modes of the p53-TAD1 (A), and SJ compounds (B-E) with respect to the binding pocket residues, Phe19, Leu22, Trp23 and Leu26 of p53-TAD1 peptide in the MdmX complexes. The positioning of these side chains in p53-TAD1 peptide in NMR (brown) and crystal structure (light green) is also shown as a reference. The distance between the C γ atoms of the compound and L22 is shown. For clarity, the piperazin moiety which is solvent exposed is not shown in the structure of the compounds.

Figure 5. Hydrogen bonds that appear in MdmX complex with the p53-TAD1 peptide are missing in the MdmX-SJ complexes

(A) Plot of back bone chemical shift difference (CSD; $\Delta\delta$) for amide proton (^1H), nitrogen (^{15}N) and carbonyl (^{13}C) between MdmX:p53-TAD1 and MdmX:SJ057 complexes versus residue number. Similar data for the other MdmX:SJ complexes are shown in Figure S5B, suggesting that these differences are observed for all the MdmX:SJ complexes and SJ057 is reported as an example. (B) Average H-bond energy plotted with respect to residue number calculated using conventional protocols²³⁻²⁵ for the p53-TAD1 and SJ057 complex. The solid black line indicates the average

value with dashed black lines representing the average standard error of the mean. (C) The standard error in arbitrary energy units (A.U.) for a given backbone amide which is hydrogen bonded ($\sigma_{\text{E-HB}}$). $\sigma_{\text{E-HB}}$ was calculated from structures solely determined by NOE restraints and therefore represents how well structural regions are defined in cases where a hydrogen bond can exist. Solid black (gold) bars represent $\sigma_{\text{E-HB}}$ that could be calculated for the MdmX:p53-TAD1 (MdmX:SJ057) complex. Gold (black) bars that show a value less than zero represent hydrogen bonds that existed in the p53-TAD1 (SJ057) complex, but not in the SJ057 (p53-TAD1) complex. Solid black and gold squares indicate a hydrogen bond was measurable, but only existed one time in the NMR bundle. Stars drawn at zero indicate proline residues. (D) Structure of the MdmX:p53-TAD1 complex with the hydrogen bonds missing in the MdmX:SJ057 complex. Donor (Receptor) atoms are depicted as spheres colored in red (gold). Hydrogen bonds that were absent in the p53-TAD1 complex, but present in the SJ057 complex are the spheres colored in blue (donor) and cyan (receptor). A grey surface representation is drawn with residues that showed a greater than one standard deviation CSD between the p53-TAD1 and SJ057 complexes are colored in light green.

Figure 6. SJ compounds activate p21 expression in retinoblastoma cell lines and in HCT116 cells in a p53-dependent manner

(A) Extent of activation of p21 expression in Weri and Y29 retinoblastoma cell lines by treatment with Nutlin-3a and the four SJ compounds. The induction of p21 by Nutlin-3a and SJ057 was similar. (B) Extent of activation of p21 expression in p53^{-/-} (light bars) and p53^{+/+} (solid bars) HCT116 cells by treatment with Nutlin-3a and the four SJ compounds. The induction of p21 by Nutlin-3a and SJ057 was similar and p53-

dependent. In both panels, the extent of p21 expression shown is the fold change relative to the DMSO control. All cells were treated with 20 μ M compound and were incubated for 20 hours before analysis of p21 expression using immunoblot staining.

Table 1. Binding affinities of p53 and SJ compounds for MdmX**(A) Binding affinities using FP assay**

Compound name (abbreviation)	IC ₅₀ (μM)	95% CI ¹ (μM)
SJ000558295-3 (SJ295)	7.0	[4.6, 10.6]
SJ000773212-2 (SJ212)	6.2	[3.7, 10.3]
SJ000801057-1 (SJ057)	8.6	[2.6, 28.5]
SJ000558298-7 (SJ298)	24.9	[6.9, 89.6]

¹Confidence limit**(B) Binding affinities from ITC**

Compound	ΔG (kcal mol ⁻¹)	ΔH (kcal mol ⁻¹)	-TΔS (kcal mol ⁻¹)	N	K _D ^{ITC} (μM)
p53	-9.3 ± 0.3	-17.5 ± 0.3	8.1 ± 0.1	0.9 ± 0.1	0.15 ± 0.04
SJ295	-7.3 ± 0.4	-6.0 ± 4.8	-1.3 ± 5.2	1.8 ± 0.4	4.7 ± 1.8
SJ212	n.d. ¹	n.d.	n.d.	n.d.	n.d.
SJ057	-8.6 ± 0.2	-3.3 ± 0.2	-5.2 ± 0.4	1.6 ± 0.2	0.6 ± 0.2
SJ298	-6.7 ± 0.2	-7.7 ± 2.0	1.0 ± 2.3	1.0 ± 0.2	12.0 ± 6.0

¹Not Determined.

All errors are derived from triplicate measurements.

(C) Binding affinities from NMR titrations

Compound	K _D ^{NMR,global} (μM) ¹	K _D ^{NMR,global} (μM) ²
SJ295	1.7 ± 1.1	6.0 ± 1.8
SJ212	0.7 ± 0.6	0.6 ± 0.6
SJ057	0.8 ± 0.7	0.6 ± 0.5
SJ298	2.4 ± 0.7	4.2 ± 1.0

¹All resonances that exceeded the minimum Δδ_{15N} and signal-to-noise criteria were used (see supplemental Experimental Procedure); ²Only resonances which fulfilled all selection criteria and that were common to all compound titrations (Val27, Arg28, Leu31, Ala39, Phe47, Met53, Gly72, and Glu73) were used.

Table 2. Statistics for the NMR-derived solution structures of MdmX:ligand complexes determined using CYANA and refined using AMBER.

Parameters	MdmX:p53-TAD1	MdmX:SJ295	MdmX:SJ212	MdmX:SJ298	MdmX:SJ057
Constraints	1457	1240	1716	1494	1663
No. of upper distance limits					
Intra-residue	421	310	402	413	445
Short range ($ i-j \leq 1$)	340	364	432	379	462
Medium range ($2 \leq i-j \leq 5$)	284	332	514	380	428
Long range ($5 < i-j $)	249	222	329	232	303
Peptide – Intra-residue	75	0	0	0	0
Inter-molecular	88	12	39	90	25
No. of dihedral angle constraints	87	87	87	87	87
No. of hydrogen bond constraints	20	20	20	20	20
Distance violations $> 0.4 \text{ \AA}$	0	0	0	0	0
Maximum violation (\AA)	0.300	0.228	0.364	0.245	0.297
No. of angle violations	0	23 ^a	1 ^a	3 ^a	6 ^a
Maximum angle violation ($^\circ$)	3.2 $^\circ$	25.8 $^\circ$	7.1 $^\circ$	17.6 $^\circ$	7.9 $^\circ$
Atomic pairwise RMSD (\AA) ^b					
Backbone atoms	0.36	0.37	0.31	0.50	0.33
Heavy atoms	0.61	0.63	0.66	0.82	0.60
Ramachandran plot statistics, residues in region (%):					
most favored	90.6	81.6	82.1	86.1	87.4
additional allowed	8.0	18.2	17.8	13.0	10.7
generously allowed	0.7	0.3	0.1	0.5	1.5
disallowed	0.7	0	0	0.4	0.4
Structure verification results (Z-score ^c):					
Verify3D	-0.32	-3.05	-0.96	-2.57	-1.12
ProsaII (-ve)	0.21	-0.99	-0.37	-1.41	-0.29
Procheck (phi-psi)	0.12	-0.90	-1.02	-0.31	-0.08
Procheck (all)	-1.06	-2.60	-2.66	-1.71	-2.13
MolProbity Clash score	1.33	1.21	1.11	1.26	1.00

^a All angle violations $> 5^\circ$ are in the near-N-terminal residues, 26—28.

^b RMSD calculated for MdmX residues 27—107 (first and last four residues excluded), and either p53 residues 18—26 or the compound.

^c With respect to mean and standard deviation for a set of 252 X-ray structures < 500 residues, of resolution $\leq 1.80 \text{ \AA}$, R-factor ≤ 0.25 and R-free ≤ 0.28 ; a positive value indicates a 'better' score. Generated using Protein Structure Validation Software Suite

PSVS 1.5 (http://psvs-1_5-dev.nesg.org). (The Z-scores for the crystal structure of MdmX:p53 complex (pdb:3DAB) using Verify3D, Prosall (-ve), Procheck (phi-psi), Procheck (all,) and MolProbity are -0.48, 0.04, 0.67, 0.77, and 0.66, respectively.)

References

- 1 Vara, B. A. *et al.* Organocatalytic, diastereo- and enantioselective synthesis of nonsymmetric cis-stilbene diamines: a platform for the preparation of single-enantiomer cis-imidazolines for protein-protein inhibition. *J. Org. Chem.* **79**, 6913-6938, (2014).
- 2 Wade, M., Li, Y. C. & Wahl, G. M. MDM2, MDMX and p53 in oncogenesis and cancer therapy. *Nat. Rev. Cancer* **13**, 83-96, (2013).
- 3 Laurie, N. A. *et al.* Inactivation of the p53 pathway in retinoblastoma. *Nature* **444**, 61-66, (2006).
- 4 Vassilev, L. T. *et al.* In vivo activation of the p53 pathway by small-molecule antagonists of MDM2. *Science* **303**, 844-848, (2004).
- 5 Popowicz, G. M., Domling, A. & Holak, T. A. The structure-based design of Mdm2/Mdmx-p53 inhibitors gets serious. *Angew. Chem. Int. Ed. Engl.* **50**, 2680-2688, (2011).
- 6 Popowicz, G. M., Czarna, A. & Holak, T. A. Structure of the human Mdmx protein bound to the p53 tumor suppressor transactivation domain. *Cell Cycle* **7**, 2441-2443, (2008).
- 7 Cavanagh, J. C., Fairbrother, W. J., Palmer, A. G. r., Rance, M. & Skelton, N. J. *Principles and Practice: Protein NMR Spectroscopy*. 2nd edn, (2007).
- 8 Sanchez, M. C., Renshaw, J. G., Davies, G., Barlow, P. N. & Vogtherr, M. MDM4 binds ligands via a mechanism in which disordered regions become structured. *FEBS Lett.* **584**, 3035-3041, (2010).
- 9 Arai, M., Ferreon, J. C. & Wright, P. E. Quantitative analysis of multisite protein-ligand interactions by NMR: binding of intrinsically disordered p53 transactivation subdomains with the TAZ2 domain of CBP. *J. Am. Chem. Soc.* **134**, 3792-3803, (2012).
- 10 Markin, C. J. & Spyropoulos, L. Accuracy and precision of protein-ligand interaction kinetics determined from chemical shift titrations. *J. Biomol. NMR* **54**, 355-376, (2012).
- 11 Phan, J. *et al.* Structure-based design of high affinity peptides inhibiting the interaction of p53 with MDM2 and MDMX. *J. Biol. Chem.* **285**, 2174-2183, (2010).
- 12 Popowicz, G. M. *et al.* Molecular basis for the inhibition of p53 by Mdmx. *Cell Cycle* **6**, 2386-2392, (2007).

- 13 Bharatham, N., Bharatham, K., Shelat, A. A. & Bashford, D. Ligand binding mode prediction by docking: mdm2/mdmx inhibitors as a case study. *J. Chem. Inf. and Mod.* **54**, 648-659, (2014).
- 14 Bottger, V. *et al.* Comparative study of the p53-mdm2 and p53-MDMX interfaces. *Oncogene* **18**, 189-199, (1999).
- 15 Hu, B., Gilkes, D. M. & Chen, J. Efficient p53 activation and apoptosis by simultaneous disruption of binding to MDM2 and MDMX. *Cancer Res.* **67**, 8810-8817, (2007).
- 16 Pazgier, M. *et al.* Structural basis for high-affinity peptide inhibition of p53 interactions with MDM2 and MDMX. *Proc. Natl. Acad. U.S.A.* **106**, 4665-4670, (2009).
- 17 Shen, Y. *et al.* Consistent blind protein structure generation from NMR chemical shift data. *Proc. Natl. Acad. U.S.A* **105**, 4685-4690, (2008).
- 18 Berjanskii, M. V. & Wishart, D. S. A simple method to predict protein flexibility using secondary chemical shifts. *J. Am. Chem. Soc.* **127**, 14970-14971, (2005).
- 19 Moon, S. & Case, D. A. A new model for chemical shifts of amide hydrogens in proteins. *J. Biomol. NMR* **38**, 139-150, (2007).
- 20 Osapay, K. & Case, D. A. A new analysis of proton chemical shifts in proteins. *J. Am. Chem. Soc.* **113**, 9436-9444, (1991).
- 21 Haigh, C. W. & Mallion, R. B. Ring current theories in Nuclear Magnetic Resonance. *Prog. in NMR Spec.* **13**, 303-344, (1980).
- 22 Neal, S., Nip, A. M., Zhang, H. & Wishart, D. S. Rapid and accurate calculation of protein ¹H, ¹³C and ¹⁵N chemical shifts. *J. Biomol. NMR* **26**, 215-240, (2003).
- 23 Mills, J. E. & Dean, P. M. Three-dimensional hydrogen-bond geometry and probability information from a crystal survey. *J. Comp-Aid Mol. Des.* **10**, 607-622, (1996).
- 24 Morozov, A. V., Kortemme, T., Tsemekhman, K. & Baker, D. Close agreement between the orientation dependence of hydrogen bonds observed in protein structures and quantum mechanical calculations. *Proc. Natl. Acad. U.S.A* **101**, 6946-6951, (2004).
- 25 Kohlhoff, K. J., Robustelli, P., Cavalli, A., Salvatella, X. & Vendruscolo, M. Fast and accurate predictions of protein NMR chemical shifts from interatomic distances. *J. Am. Chem. Soc.* **131**, 13894-13895, (2009).
- 26 Borchers, W. *et al.* Disorder and residual helicity alter p53-Mdm2 binding affinity and signaling in cells. *Nat. Chem. Biol.* **10**, 1000-1002, (2014).

- 27 Fry, D. C. *et al.* NMR structure of a complex between MDM2 and a small molecule inhibitor. *J. Biomol. NMR* **30**, 163-173, (2004).
- 28 Spolar, R. S. & Record, M. T., Jr. Coupling of local folding to site-specific binding of proteins to DNA. *Science* **263**, 777-784, (1994).
- 29 Lacy, E. R. *et al.* p27 binds cyclin-CDK complexes through a sequential mechanism involving binding-induced protein folding. *Nat. Struct. Mol. Biol.* **11**, 358-364, (2004).
- 30 Michelsen, K. *et al.* Ordering of the N-Terminus of Human MDM2 by Small Molecule Inhibitors. *J. Am. Chem. Soc.* **134**, 17059-17067, (2012).
- 31 Freire, E. A thermodynamic approach to the affinity optimization of drug candidates. *Chem. Bio. & Drug Des.* **74**, 468-472, (2009).

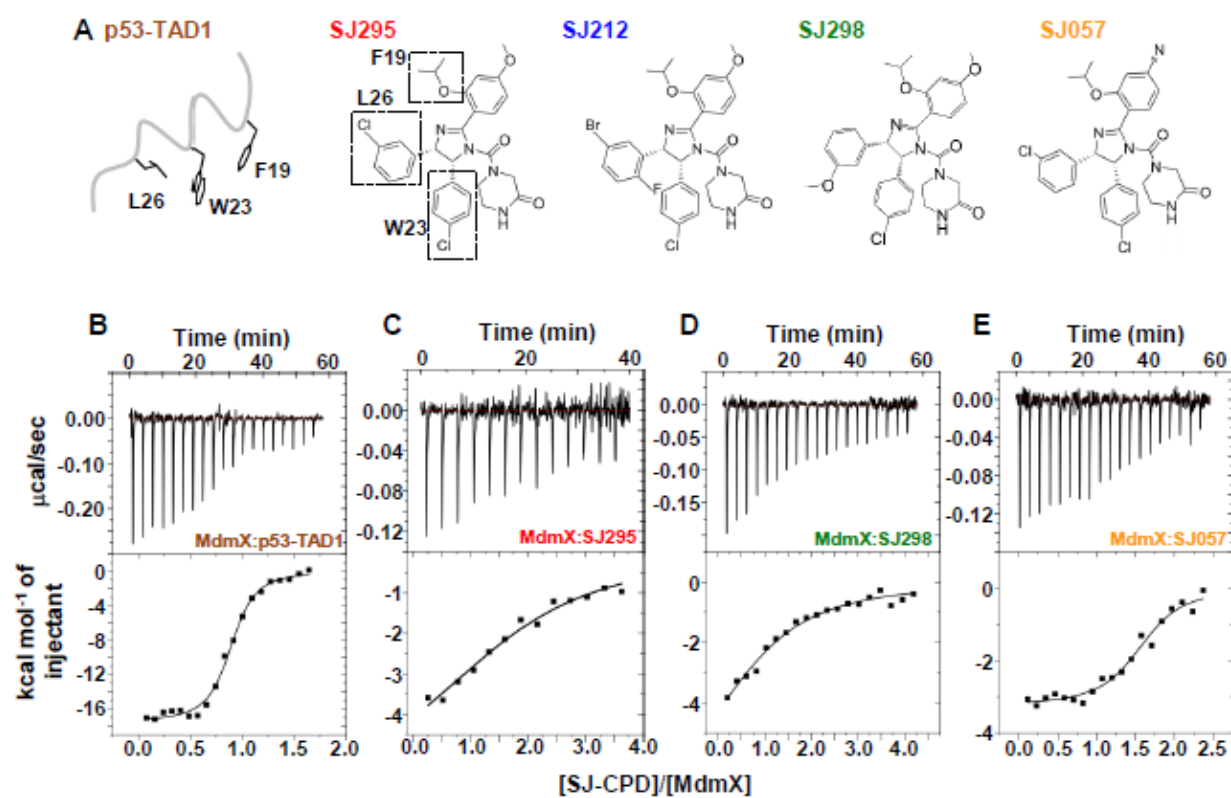


Figure 1

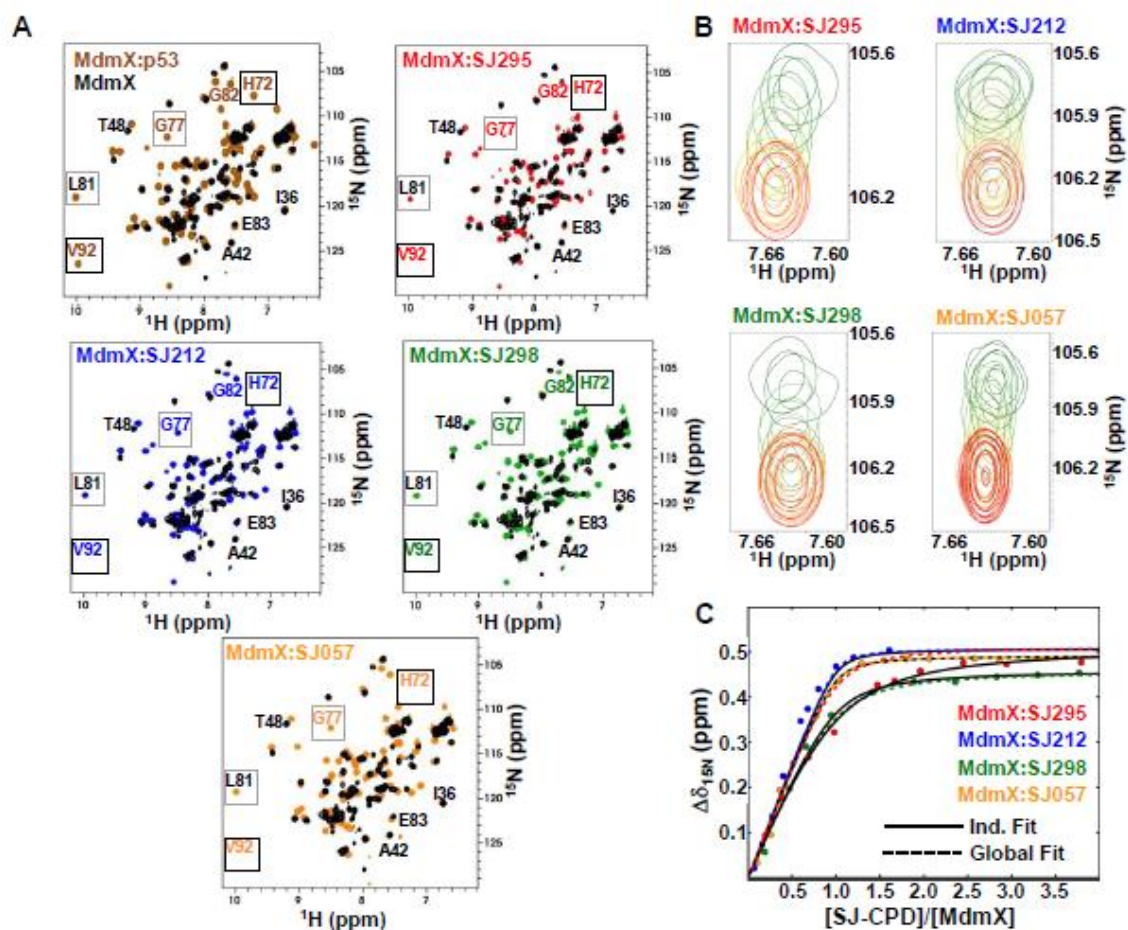


Figure 2

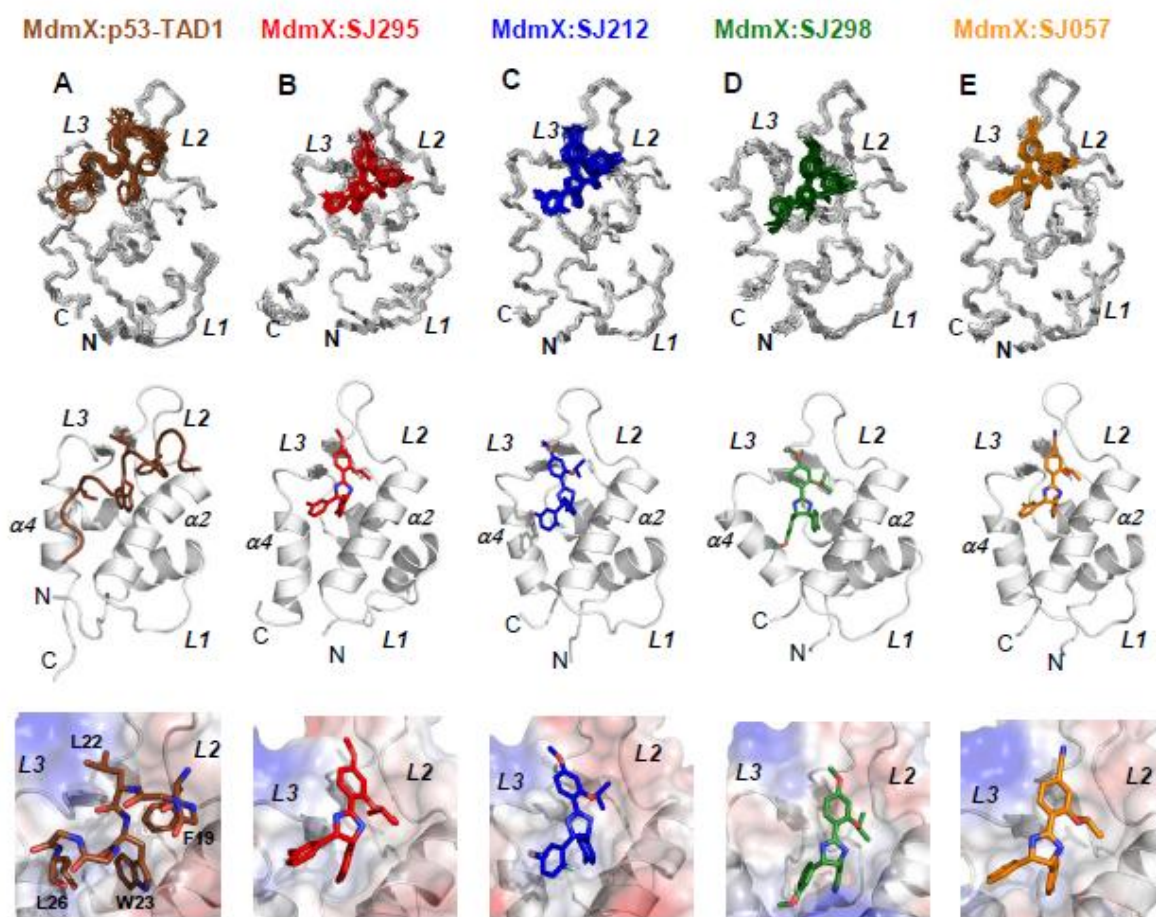


Figure 3

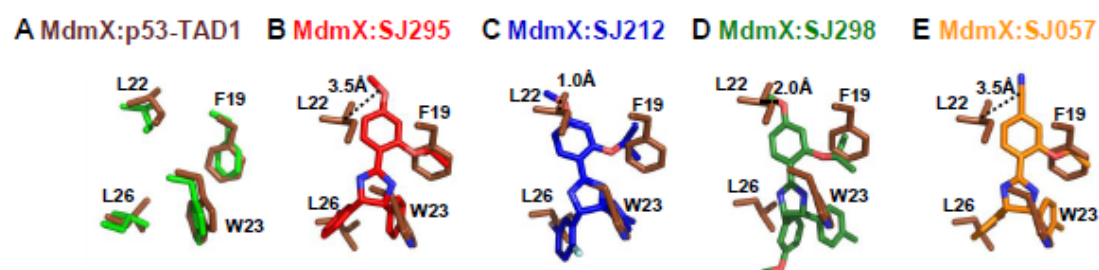


Figure 4

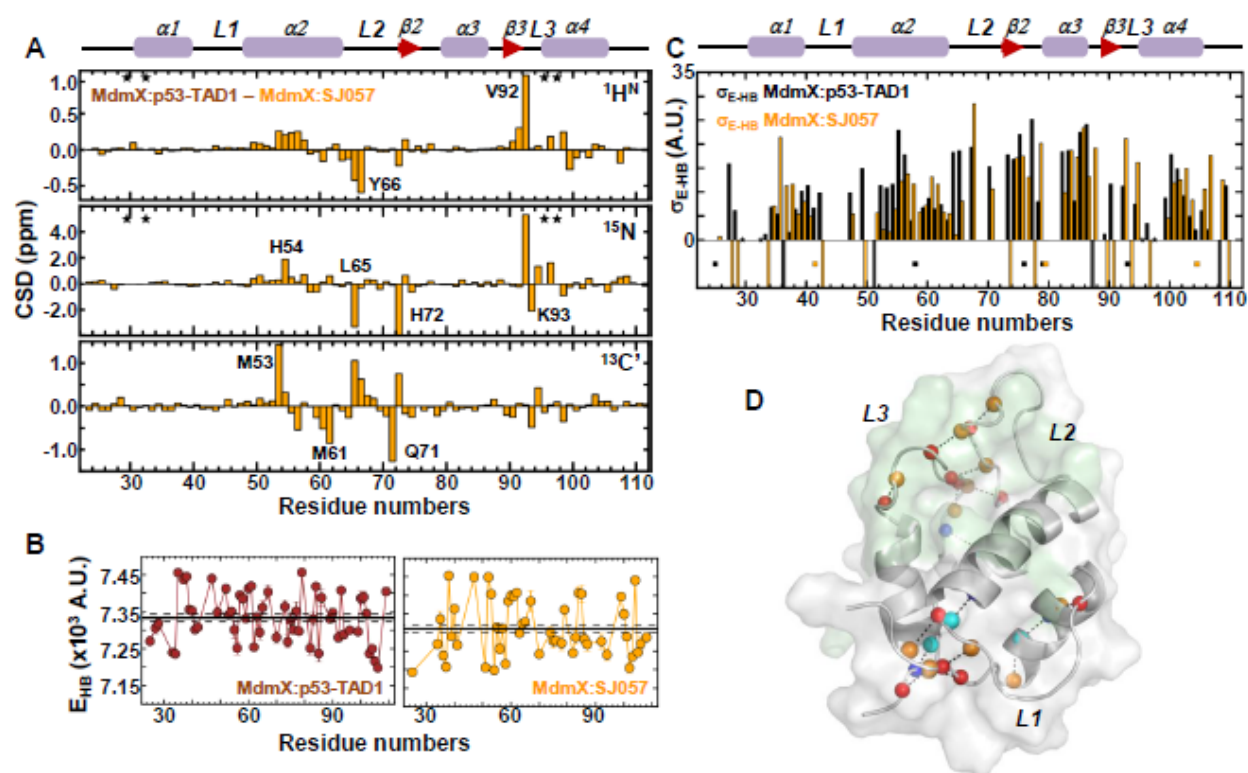


Figure 5

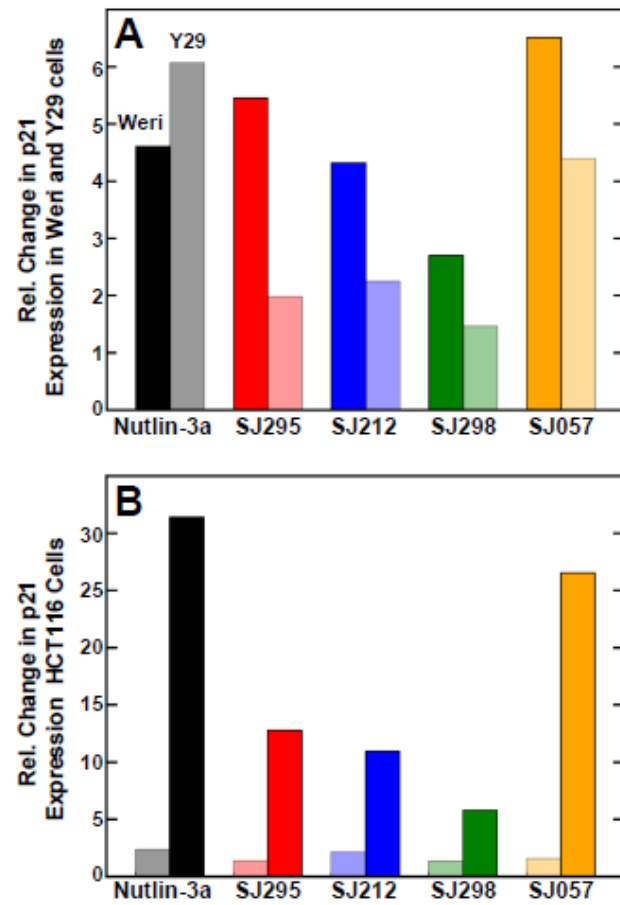
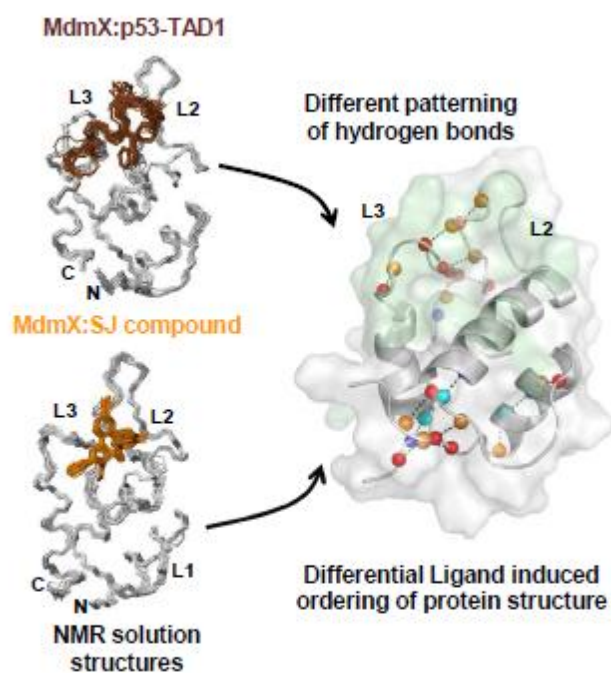


Figure 6



Graphical abstract

Research Highlights

We present a thermodynamic characterization of Nutlin analogs that bind better to MdmX than Nutlin-3a.

First solution NMR structures of MdmX in complex with small molecule Nutlin analogs.

Structures report differential ordering by displaying different patterns in hydrogen bonds.

The reported Nutlin analogs activated p53 and induced p21^{Cip1} expression in retinoblastoma cell lines.